

Hot-Chemistry Structural Phase Transformation in Single-Crystal Chalcogenides for Long-Life Lithium Ion Batteries

Fathy M. Hassan,^{†,‡} Qianqian Hu,[†] Jing Fu,[†] Rasim Batmaz,[†] Jingde Li,[†] Aiping Yu,[†] Xingcheng Xiao,^{*,‡} and Zhongwei Chen^{*,†}

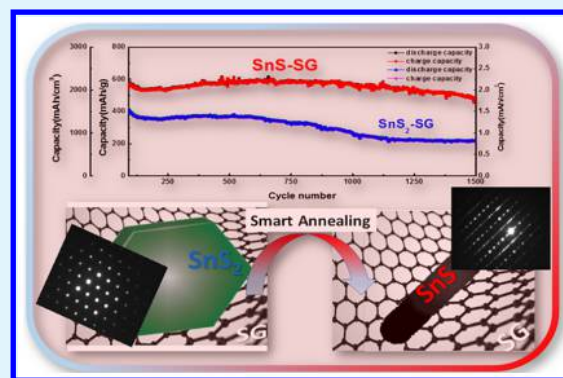
[†]Department of Chemical Engineering, Waterloo Institute for Nanotechnology, and Waterloo Institute for Sustainable Energy, University of Waterloo, Waterloo, Ontario N2L 3G1, Canada

[‡]Chemical and Materials Systems, General Motors Global Research and Development Center, Warren, Michigan 48090, United States

S Supporting Information

ABSTRACT: Tuned chalcogenide single crystals rooted in sulfur-doped graphene were prepared by high-temperature solution chemistry. We present a facile route to synthesize a rod-on-sheet-like nanohybrid as an active anode material and demonstrate its superior performance in lithium ion batteries (LIBs). This nanohybrid contains a nanoassembly of one-dimensional (1D) single-crystalline, orthorhombic SnS onto two-dimensional (2D) sulfur-doped graphene. The 1D nanoscaled SnS with the rodlike single-crystalline structure possesses improved transport properties compared to its 2D hexagonal platelike SnS₂. Furthermore, we blend this hybrid chalcogenide with biodegradable polymer composite using water as a solvent. Upon drying, the electrodes were subjected to heating in vacuum at 150 °C to induce polymer condensation via formation of carboxylate groups to produce a mechanically robust anode. The LIB using the as-developed anode material can deliver a high volumetric capacity of ~2350 mA h cm⁻³ and exhibit superior cycle stability over 1500 cycles as well as a high capacity retention of 85% at a 1 C rate. The excellent battery performance combined with the simplistic, scalable, and green chemistry approach renders this anode material as a very promising candidate for LIB applications.

KEYWORDS: high-temperature solution chemistry, polymer condensation, lithium ion batteries, chalcogenides, DFT calculation



INTRODUCTION

The excessive consumption of fossil fuel leads lithium ion batteries (LIBs) to a vital role as renewable energy storage devices for applications of electric vehicles and portable electronics. Commercial LIBs employ graphite as the anode material with a theoretical capacity of 372 mA h g⁻¹, which cannot satisfy the energy demand for the advance of new technology. Therefore, it is highly required to develop new anode materials with high capacity and reliability as well as low fabrication cost for practical applications.^{1–15} Recently, chalcogenides have attracted significant attention to the field of energy-harvesting technology, including solar cells, batteries, and supercapacitors.^{16–21} Particularly, nanostructured layered metal chalcogenides have been developed for LIBs²² due to their unique physical and chemical properties and large contact area beneficial to Li⁺²³ or Na⁺²⁴ storage. Tin sulfides (SnS_x) are the anode materials of choice, owing to their almost 2-fold higher specific capacity than that of commercial graphite.²⁵ Two steps are involved during their charge and discharge processes: conversion and lithium alloying reactions. The conversion of SnS_x leads to the formation of Li₂S along with a solid electrolyte interphase (SEI) layer, resulting in an

irreversible capacity loss, while the alloying/dealloying process contributes to the reversible capacity.^{26–28} However, SnS_x materials generally suffer from large volume changes and aggregation during the alloying/dealloying process, causing severe mechanical degradations of the electrodes and thus the resultant poor cycle performance.²⁹ Significant efforts have been devoted to addressing this challenge through engineering SnS_x-based electrodes at the nanoscale. In spite of tremendous work on the morphologies of SnS_x, however, few have reported sufficient long-term cycling stability in LIBs.^{30–33}

Solutions at high temperature and pressure undergo dramatic changes in density and dielectric constants, and new reaction pathways become accessible.^{34,35} Solvothermal synthesis has become a powerful approach toward fabricating nanomaterials with high quality, reproducibility, and a controlled shape property.^{36–38} Herein we report a novel method to synthesize one-dimensional (1D) orthorhombic single crystals of SnS rooted in sulfur-doped graphene (denoted as SnS-SG),

Received: March 29, 2017

Accepted: May 30, 2017

Published: May 30, 2017

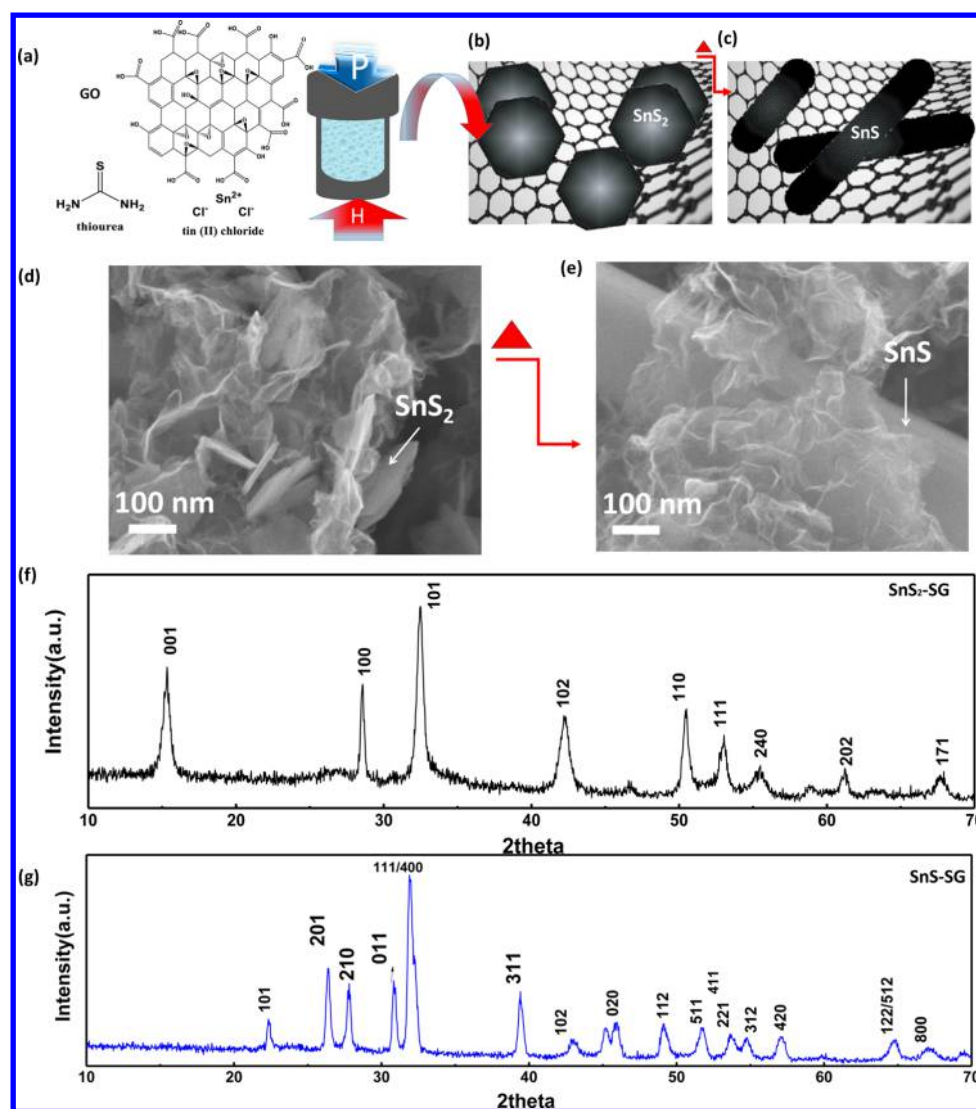


Figure 1. (a) Schematic of the hot-chemistry synthesis. Illustrations of the (b) hexagonal SnS_2 nanoplates and (c) SnS nanorods supported on SG, and the corresponding SEM images of (d) SnS_2 -SG and (e) SnS -SG. XRD analyses of (f) SnS_2 -SG and (g) SnS -SG.

forming a unique rod-on-sheet-like structure. The 1D SnS nanorod derives from a structural phase transformation through a post thermal annealing of a two-dimensional (2D) hexagonal platelike SnS_2 with the support of sulfur-doped graphene (SG). The SG provides numerous nucleation sites that can anchor the SnS firmly through a strong covalent synergy in the SnS -SG nanohybrid. Such synergistic coupling between the SnS and SG can not only boost the Li^+ storage in terms of a higher capacity than that of SnS , but also enhance the cycling stability in LIBs significantly. The SnS -SG nanohybrid exhibited a large initial capacity of 1630 mA h g^{-1} and long cycle stability over 1500 cycles with a high capacity retention of 85%. Such outstanding performance gives SnS -SG high promise in practical applications of high-capacity and durable LIBs.

RESULTS AND DISCUSSION

The concept of structural phase change from 2D hexagonal SnS_2 to 1D orthorhombic SnS is shown schematically in Figure S1 (Supporting Information). The structural evolution of SnS -SG involves two steps: (i) the high-temperature solution chemistry synthesis of SnS_2 supported on a sulfur-doped graphene nanocomposite (denoted as SnS_2 -SG) and (ii) the

chemical structure transition from SnS_2 -SG to SnS -SG via thermal annealing at 500°C . During the synthesis of SnS_2 -SG, graphene oxides (GOs), with several oxygenated functional groups, attract Sn^{2+} , which is oxidized by GOs via high-temperature and high-pressure chemistry known as the solvothermal reaction, forming a platelike structure (Figure 1a).^{37,39,40} A subsequent thermal annealing process at 500°C chemically transfers the structure of the as-prepared SnS_2 , where the high temperature drives the SnS_2 nanoplates to curve and grow longitudinally, resulting in a rodlike structure (Figure 1b-e).

The morphologies of the SnS_2 -SG and SnS -SG nanocomposites were characterized by scanning electron microscopy (SEM). As shown in Figure 1d, the SnS_2 nanoplates are nested uniformly in the SG layers and wrinkles. After the annealing process, the SnS_2 nanoplates were converted to the rodlike SnS anchored on the SG sheets (Figure 1e). The crystal structures of the SnS_2 -SG and SnS -SG nanohybrids were further characterized by X-ray diffraction (XRD) (Figure 1f,g), which can be indexed to the single-crystalline hexagonal SnS_2 (JCPDS no. 01-1010)⁴¹ and orthorhombic SnS (JCPDS no. 39-0354),^{41,42} respectively. In addition, no obvious peaks from

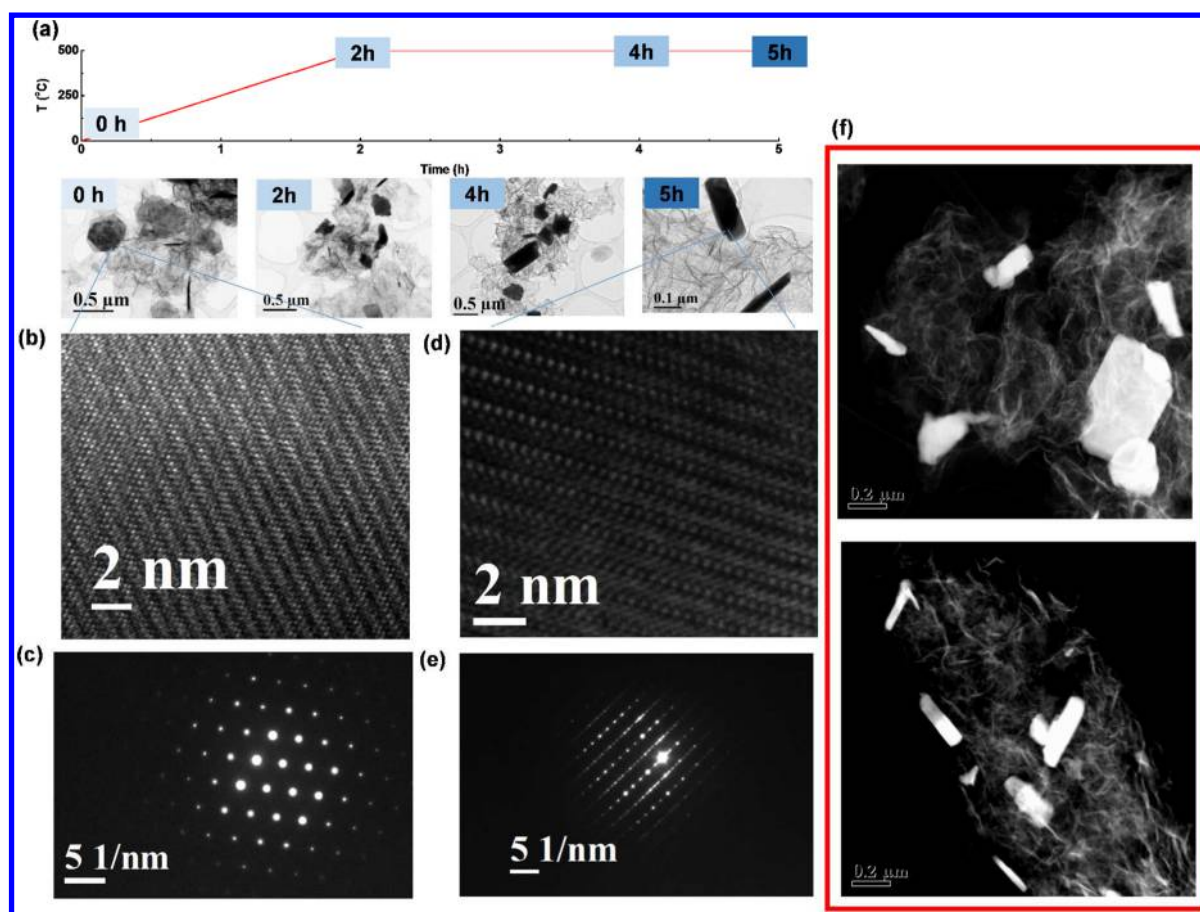


Figure 2. (a) Stepwise phase changes from single-crystal hexagonal SnS_2 to rodlike orthorhombic SnS with increasing temperature. (b) HRTEM image of the hexagonal nanosheets at 0 h and (c) the corresponding SAED pattern, which clearly reveal the single-crystalline, hexagonal SnS_2 . (d) HRTEM image of the orthorhombic nanorods at 5 h and (e) the corresponding SAED pattern, which clearly indicate the single-crystalline, orthorhombic SnS . (f) HAADF-STEM images capturing the curving of SnS_2 nanoplates on SG and the subsequent conversion to nanorods of SnS on SG.

impurities can be found in SnS-SG , indicating the full reduction of Sn^{4+} and the resultant chemical conversion from SnS_2 to SnS .

The stepwise structural transformation to the rodlike orthorhombic SnS with increasing temperature is illustrated in Figure 2a. As the temperature increased to 500 °C in 2 h, the hexagonal SnS_2 nanoplates (0 h) started to reconstruct their structure with in-plane distortion. After the temperature was held at 500 °C for 2 h, the SnS_2 nanoplates curved and grew longitudinally, resulting from surface diffusion of SnS_2 on the SG nanosheets with simultaneous loss of sulfur. Accordingly, the SnS_2 nanoplates were completely transformed into a rodlike structure after 5 h. The signs of curving of the nanoplates and subsequent conversion into nanorods is demonstrated by the high-angle annular dark field (HAADF) scanning transmission electron microscopy (STEM) image in Figure 2f.

The high-resolution transmission electron microscopy (HRTEM) image of the hexagonal SnS_2 nanoplates (Figure 2b) and selected area electron diffraction (SAED) pattern (Figure 2c) clearly reveal a hexagonal single-crystal structure of SnS_2 . The element distribution in $\text{SnS}_2\text{-SG}$ is demonstrated by the HAADF-STEM image (Figure S2a, Supporting Information) followed by energy-dispersive X-ray spectroscopy (EDS) color mapping of the element distribution (Figure S2b–e). Figure 2d displays an HRTEM image of the orthorhombic nanorods, and its corresponding SAED pattern is shown in

Figure 2e, indicating an orthorhombic single-crystal structure of SnS . In this regard, SG plays a significant role as a supporter and morphology regulator during the synthesis of $\text{SnS}_2\text{-SG}$ and SnS-SG nano hybrids. SG, possessing a layered structure with flexibility, can offer accommodations for the SnS_2 and SnS to embed and prevents the resultant crystal structures from growing disorderly and unsystematically. Parts f and g of Figure S2 show the SEM images of SnS_2 and SnS synthesized under the same solvothermal synthesis conditions and subsequent annealing procedures without being supported on SG. Distinct morphology changes of both the SnS_2 and SnS can be observed compared to $\text{SnS}_2\text{-SG}$ and SnS-SG . The SEM images of both the SnS_2 and SnS without being supported on SG present their booming aggregation into bulky particles, suggesting that SG plays a vital role in controlling crystal structures in terms of $\text{SnS}_2\text{-SG}$ and SnS-SG .

Figure 3a shows the survey spectrum of X-ray photoelectron spectroscopy (XPS) analysis of $\text{SnS}_2\text{-SG}$ and SnS-SG nano hybrids, indicating the presence of the elements C, S, Sn, and O. The C 1s high-resolution XPS spectra of $\text{SnS}_2\text{-SG}$ and SnS-SG are shown in Figure 3b,c, respectively. The C 1s peak, centered at 284.8 eV, represents the C–C bonding from the highly conductive graphene materials. The broad peak with an asymmetric tail toward higher binding energy of C 1s indicates enriched sp^2 carbon. On the other hand, for SnS-SG the C 1s peak has less width and is more symmetric in shape

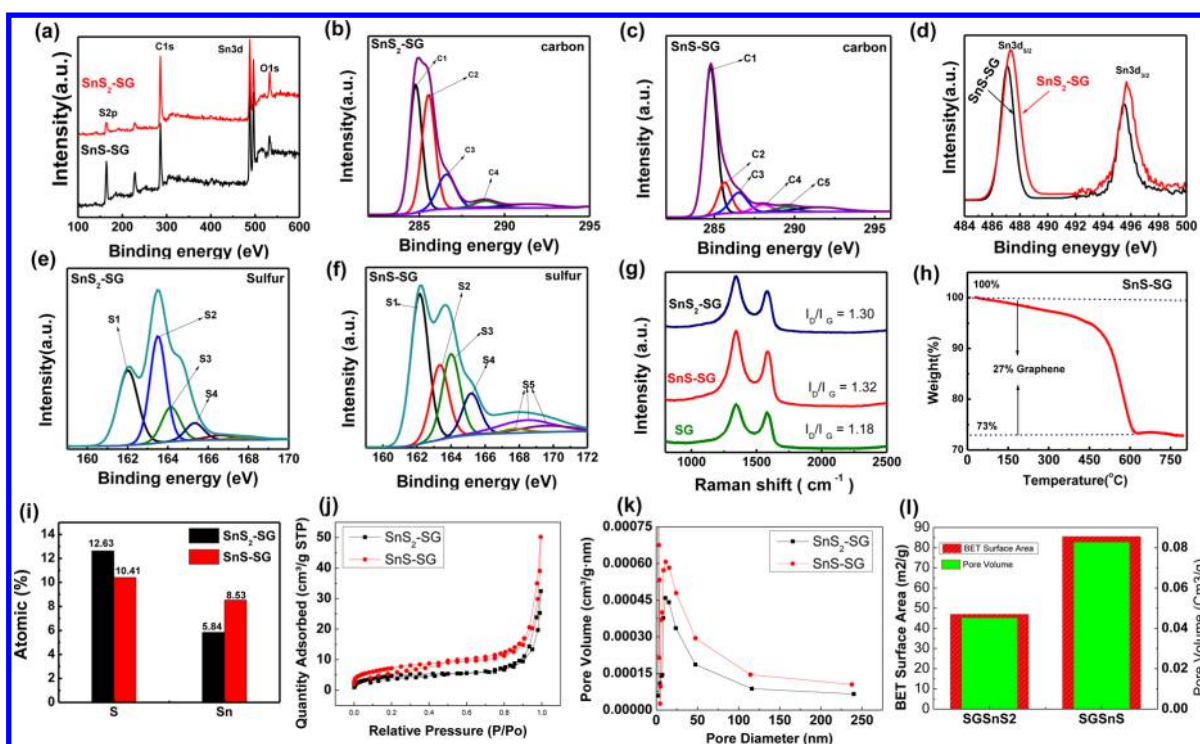


Figure 3. (a) XPS analysis showing the survey spectra of SnS₂-SG and SnS-SG. (b) and (c) are the high-resolution XPS spectra of C 1s for SnS₂-SG and SnS-SG, respectively. (d) High-resolution XPS spectra of Sn 3d demonstrating the downshift in the binding energy for the transformation from SnS₂-SG to SnS-SG. (e, f) High-resolution XPS spectra for S 2p for SnS₂-SG and SnS-SG, respectively. (g) Raman spectra of SnS₂-SG, SnS-SG, and SG. (h) TGA of SnS-SG and (i) the atomic percentage of the elements S and Sn in SnS₂-SG and SnS-SG. (j) BET adsorption isotherm, (k) pore volume, and (l) comparison of the surface area and pore volume for SnS₂-SG and SnS-SG.

with a slight shift to higher binding energy. This observation indicates a relatively low content of sp² carbon.⁴³ On this basis, we may attribute the decrease in sp² carbon to the covalent interaction of the SnS with the carbon in SG. Sn 3d high-resolution XPS of SnS-SG (Figure 3d) shows a downshift in the binding energy of both Sn 3d_{5/2} and Sn 3d_{3/2}, compared to those of SnS₂-SG. These shifts are due to losses of sulfur (SnS₂ to SnS) and decreases of the oxidation state of Sn. High-resolution XPS spectra of SnS₂-SG and SnS-SG for sulfur are also shown in Figure 3e,f, respectively. Sulfur has two main peaks for the S 2p doublet corresponding to C-S-C, where S 2p_{3/2} and S 2p_{1/2} spin-orbit coupled peaks are located at 163.98 (S3) and 165.18 eV (S4), indicative of sulfur doping in graphene.⁴⁴ The peak observed at 162.15 eV is attributed to the bonding of Sn to sulfur.⁴⁵ At higher energy, the peaks denoted as S5 are related to oxygen bound to sulfur (-SO_x).⁴⁴ The physicochemical characterization of the support SG in the absence of any Sn material is conducted by SEM, EDS, TEM, and XPS (Figure S3, Supporting Information). SG maintains the usual feature of crinkled nanosheets, and the sulfur content is estimated to be ~5.5 mass %. XPS showed the C-S-C doublet at binding energies of 163.9 and 165.2, in addition to a few at higher binding energies, revealing a few oxidized sulfurs. The structures of the SnS₂-SG, SnS-SG, and SG were further investigated by Raman spectroscopy, as shown in Figure 3g. Two peaks, located at around 1583 cm⁻¹ (G band) and 1320 cm⁻¹ (D band), are observed from SG, SnS₂-SG, and SnS-SG, corresponding to the vibration of graphitic layers and the defects and disorder of graphitic layers, respectively.⁴⁶ The intensity ratio of D to G (I_D/I_G) is determined to be 1.18, 1.30, and 1.32 for SG, SnS₂-SG, and SnS-SG, respectively. The observed increase in I_D/I_G is mainly due to the exfoliation of

graphene and the insertion of tin sulfides into SG layers.⁴⁷ The composition of SnS-SG was determined by thermogravimetric analysis (TGA). As shown in Figure 3h, the main mass loss ranging from 450 to 600 °C is attributed to the removal of graphene materials. The graphene content is calculated to be around 27%. The S/Sn ratio was further determined by EDS in Figure 3i. The S/Sn ratios of SnS₂-SG and SnS-SG are both slightly higher than those of SnS (1:1) and SnS₂ (2:1). The higher S/Sn ratios indicate sulfur doping in graphene during the reaction process. We analyzed the Brunauer-Emmett-Teller (BET) surface area and the pore volume (Figure 3j-l), as the structure transforms from SnS₂-SG to SnS-SG. It can be seen that SnS-SG attained a higher surface area and larger pore volume compared with SnS₂-SG (Figure 3l).

Electrodes for coin cell testing have been fabricated via the green chemistry route using nontoxic, and biodegradable, carboxymethyl cellulose/poly(acrylic acid) (CMC/PAA) as the binder^{48,49} and water as the solvent. The electrochemical performances were carried out by galvanostatic discharge and charge processes. Figure 4a exhibits the representative galvanostatic voltage profiles of SnS-SG for the first, second, and third cycles. SnS-SG delivers an initial discharge capacity of 1630 mA h g⁻¹ and retains 1132 mA h g⁻¹ for the first charging process with a Coulombic efficiency of 69.4%. In all of our measurements, we used the total mass of SnS_x and SG in calculating the capacity. The large irreversible capacity is mainly due to the conversion reaction of SnS with Li⁺, forming Sn and Li₂S, in addition to the formation of the SEI layer.^{26,27} However, SnS-SG shows an excellent cycling stability after the initial few cycles. As shown in Figure 4b, SnS-SG can retain a reversible capacity of around 850 mA h g⁻¹ after 200 cycles with a high Coulombic efficiency of 97%, slightly higher than

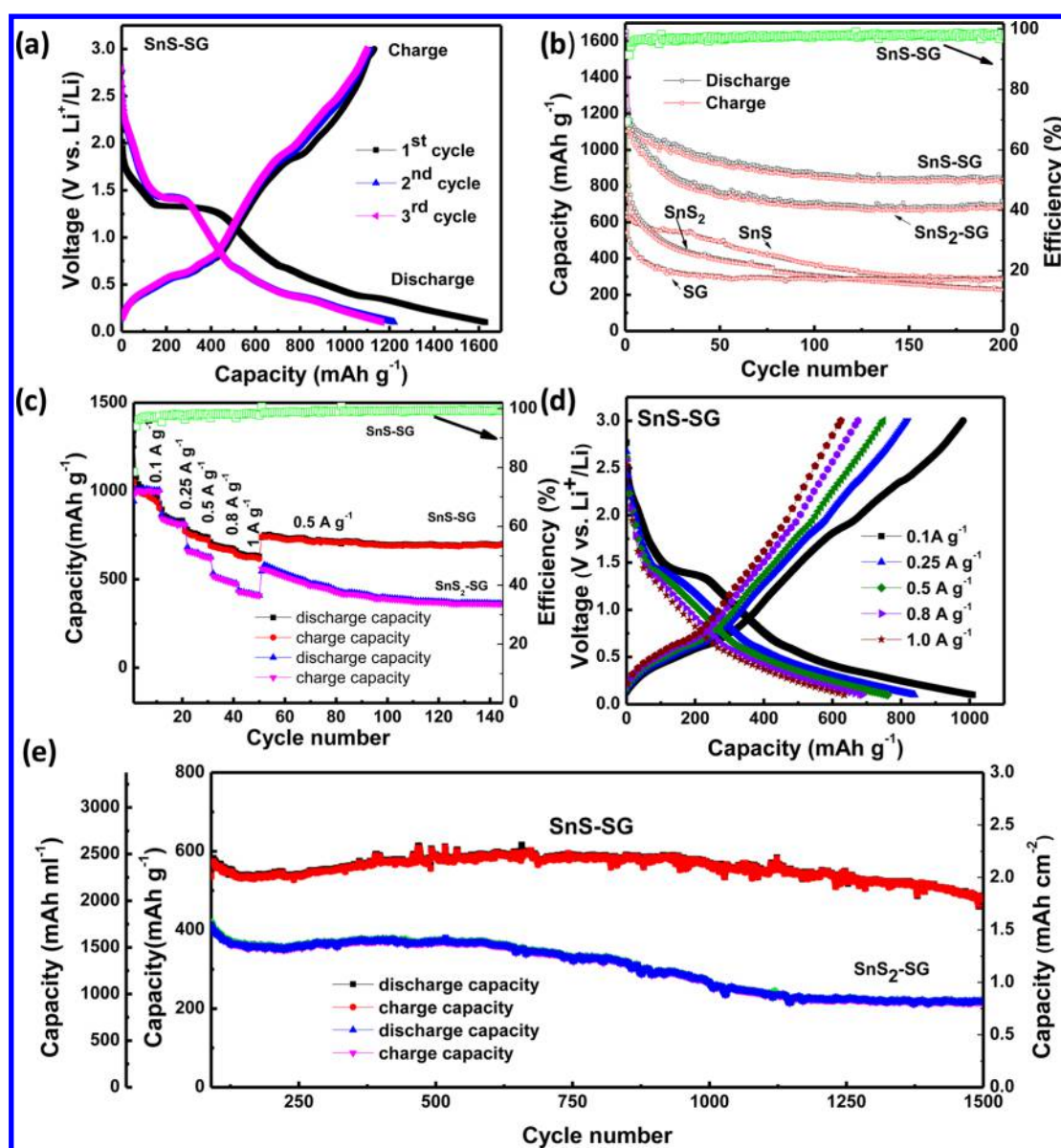


Figure 4. (a) Galvanostatic discharge and charge curves of SnS-SG. (b) Cycle stabilities of SnS₂-SG, SnS-SG, SnS₂, SnS, and SG at a current rate of 0.1 A g⁻¹. (c) Rate capabilities of SnS₂-SG and SnS-SG at different current densities. (d) Fifth cycle discharge and charge capacities of SnS-SG at different current densities. (e) Cycling stabilities of SnS₂-SG and SnS-SG at 0.5 A g⁻¹ (1 C).

the estimated theoretical capacity of SnS (782 mA h g⁻¹). The outstanding performance of SnS-SG is attributed to its high theoretical capacity and the synergistic effect of SG and SnS, which can store more lithium. It is noteworthy to mention that the synergistic effect when coupling SnS with SG, leading to higher capacity, is attributed to the ability of SG, having defects and sulfur as a dopant, to store lithium in the form of a surface adsorption reaction.⁵⁰ In sharp contrast, SnS₂-SG, SnS₂, SnS, and SG show much lower initial capacities of 1050, 752, 629, and 550 mA h g⁻¹, respectively, and subsequently faster capacity decay. For instance, only 200 and 300 mA h g⁻¹ can be achieved for SnS₂ and SnS without being supported on SG, after 200 cycles, respectively. The fast capacity decay in SnS₂ and SnS can be attributed to the fact that SnS₂ and SnS tend to agglomerate without SG as the support (confirmed in Figure S2, Supporting Information), providing less reactivity for the Li⁺ alloying/dealloying process.

Moreover, we studied the rate performance of Sn-SG, SnS₂-SG, SnS, SnS₂, and SG (Figure 4c; Figure S4, Supporting Information). SnS-SG possesses much better rate performance than SnS₂-SG, SnS₂, SnS, and SG in terms of the higher capacity and slower capacity decay. After performance of the rate capability test, the cells were allowed to recover at a lower rate of 0.5 A g⁻¹. SnS-SG recovers with high stability at an average capacity of ~700 mA h g⁻¹, while SnS₂-SG slightly decays before eventually stabilizing at ~360 mA h g⁻¹. The rate performance of SnS-SG was further investigated at higher rates, Figure S4b. The electrode delivered a capacity of 600 mA h g⁻¹ at 3.0 A g⁻¹. Subsequently, it showed a little lower charge capacity of 560 mA h g⁻¹ at 5.0 A g⁻¹ with a slight decay. However, the cell recovers on cycling at 1.5 A g⁻¹, providing a stable cycling at a charge capacity of 580 mA h g⁻¹ for up to 120 cycles.

As shown in Figure 4d, the fifth cycle discharge capacities of 1000, 830, 750, and 700 mA h g⁻¹ can be obtained at current

densities of 0.1, 0.25, 0.5, and 0.8 A g⁻¹, respectively. The voltage profile of different materials is displayed in Figure S5 (Supporting Information), while the voltage profile at different rates for SnS₂-SG is displayed in Figure S6 (Supporting Information). Even at a very high current density of 1.0 A g⁻¹ (2 C), SnS-SG still provides a capacity of 620 mA h g⁻¹, showing a superior rate capability. The excellent long life cycling stability of SnS-SG was further studied at a high current density of 0.5 A g⁻¹ (1 C). As shown in Figure 4e, a discharge capacity of 600 mA h g⁻¹ after 1000 cycles and 550 mA h g⁻¹ after 1500 cycles can be achieved at a current density of 0.5 A g⁻¹. It is important to emphasize that the capacity in terms of area and/or volume is very relevant from the practical point of view. It is interesting to note that the SnS-SG electrode material is able to deliver an areal capacity of ~2.0 mA h cm⁻² and a volumetric capacity of ~2350 mA h cm⁻³. The latter is more than 4 times greater than that of graphite used in the current LIB technology.⁵¹ By comparison, SnS₂-SG delivers a significantly lower capacity of around 200 mA h g⁻¹ after 1500 cycles with a faster capacity decay. To our best knowledge, this is the longest cycle with excellent stability for SnS-based composites,^{30,32,52,53} which is attributed to the 1D single-crystal structure of SnS and the unique design of SnS wrapped with SG. The anisotropic 1D coupled with the single-crystal structure of SnS nanorods not only possesses facile strain relaxation, leading to an improved mechanical stability, but also shortens the Li⁺ diffusion paths and electron transport length. Additionally, SG plays a key role in providing a 2D electron transport pathway and large contact sites for SnS.⁵ More importantly, SG can provide buffer space to suppress the volume changes of SnS during the Li⁺ alloying/dealloying process, maintaining the integrity of the electrode. Further discussion on the electrochemical behavior of the lithiation and delithiation has been explored by cyclic voltammetry and electrochemical impedance spectroscopy as shown Figure 5. The cyclic voltammetry (CV) curves for SnS-SG, SnS₂-SG, and SG are shown in Figure 5a-c, respectively. The Li⁺ insertion/deinsertion mechanism can be proposed as follows:

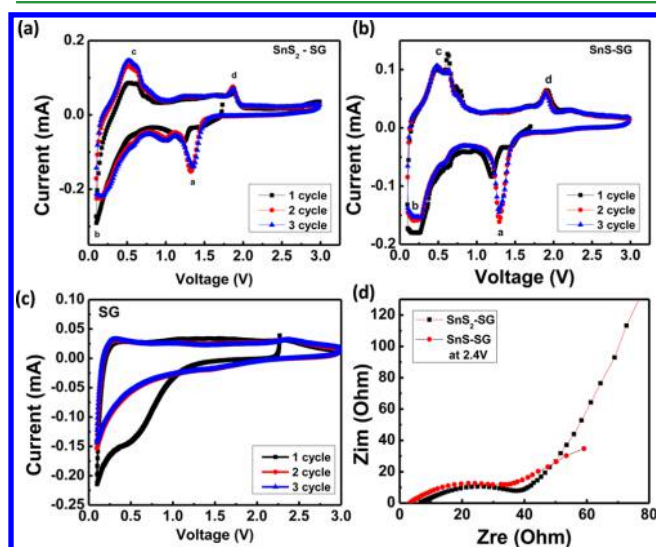
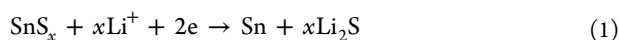


Figure 5. Cyclic voltammograms for (a) SnS-SG, (b) SnS₂-SG, and (c) SG. (d) Electrochemical impedance spectra of SnS-SG (red) and SnS₂-SG (black) with a frequency range of 1 MHz to 0.1 Hz.



As shown in Figure 5a,b, two reduction peaks are observed in the cathodic scans. The peak at around 1.3 V (a) is ascribed to the decomposition of SnS_x to Sn and Li₂S, which may result in a large irreversible capacity for the first cycle, as shown in eq 1. The second dominant peak at around 0.05 V (b) is known to arise from the formation of Li_xSn alloys as in eq 2.⁵⁴ During the anodic process, at the peak at about 0.5 V (c), Li_xSn encounters a delithiation process. It is clear that there is another anodic peak at about 1.8 V, indicating that tin may react with Li₂S to form the SnS_x phase.⁵⁴⁻⁵⁷ With regard to the second and third cycles, there are no noticeable losses of the area, providing the good stability of the electrodes. As shown in Figure 5c, for SG, in the first cycle, there are two cathodic peaks located at 0.6 and 0.1 V. The peak at ~0.6 V is related to the formation of the SEI, leading to the large irreversible capacity for the first cycle. The second peak at ~0.1 V represents the intercalation of Li⁺ into the SG layers.

To explain why SnS_x-SG nanocomposites have different features, electrochemical impedance spectroscopy (EIS) measurement of the as-prepared electrodes was conducted. Nyquist plots obtained from EIS of the SnS_x-SG samples are shown in Figure 5d. The coin cells were cycled for 10 cycles and then were charged to a potential of 2.4 V to study the internal resistance status of both electrodes. Compared with SnS₂-SG, the annealed sample (SnS-SG) has a lower initial interfacial resistance and higher charge transfer rate. We used HAADF-STEM to image the electrode structure after cycling and map the composition by energy-dispersive X-ray spectroscopy, Figure 6. This technique is sensitive to the atomic weight

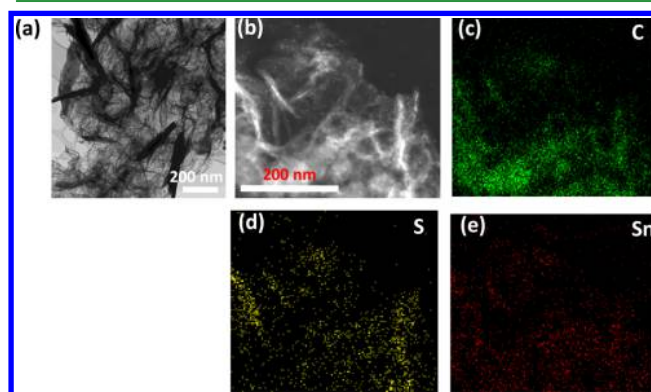


Figure 6. (a) TEM image of the SnS-SG electrode material before battery cycling, (b) HAADF-STEM image of the electrode material of a cell fabricated using SnS-SG and cycled 1500 times. (c-e) Corresponding EDS color mapping for carbon, sulfur, and tin, respectively.

of the elements, where the heavy element is shown brighter than the lighter one. The nanorods of SnS should change physically and chemically after cycling (eqs 1 and 2). However, they are still confined in the wrinkles of SG. The binder created a nestlike structure that helped the electrode material to be confined while being supported by the SG. We believe this robust structure helped the electrode to cycle 1500 times without significant loss of the capacity. The stronger covalent synergy between SnS and SG possibly leads to the excellent battery performance of SnS-SG compared to SnS₂-SG. In this regard, it is interesting to further understand the nature of the interaction between SnS_x and SG. We used quantum

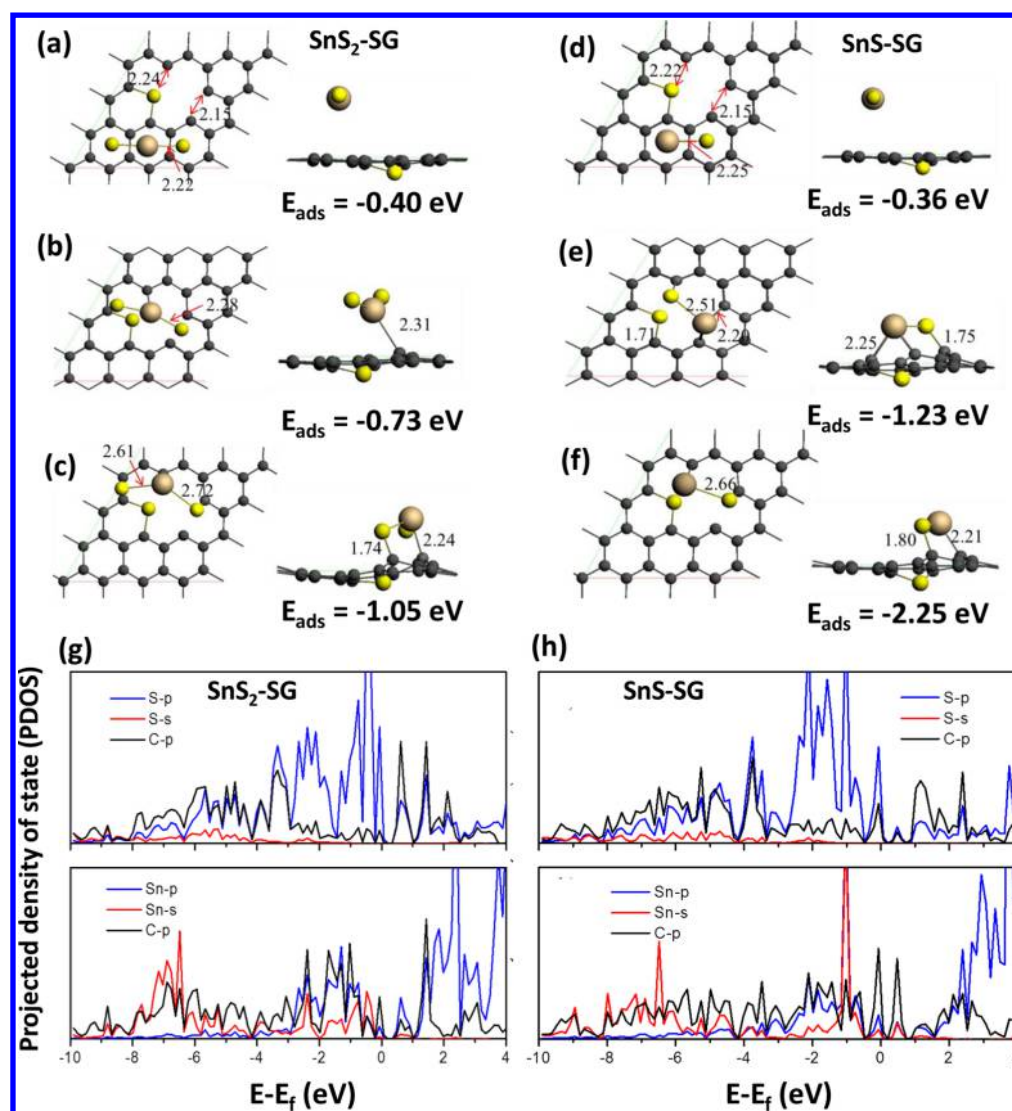


Figure 7. Geometries of the optimized SnS₂ (a–c) and SnS (d–f) adsorption configurations on SG (small gray, C; brown, Sn; yellow, S.). Projected density of states (PDOS) for Sn, S, and the individual C atoms involved in SnS₂ (g) and SnS (h) adsorption on SG for the configurations in (c) and (f), respectively.

mechanical density functional theory (DFT) calculation to model the nanocomposite structure. This is widely applied to catalysis applications and produces reliable energetics on graphene systems.^{58–60}

The DFT calculations were carried out using the program BAND,^{61,62} where the electron wave functions were developed on a basis set of numerical atomic orbitals (NAOs) and of Slater type orbitals (STOs). The triple polarization (TZP) basis of Slater-type orbitals was used. The calculations were performed by using the PBE-D3⁶³ generalized gradient approximation (GGA) for the exchange and correlation energy terms, explicitly taking into account the dispersion correction. In the present study, a 4 × 4 supercell of graphene was selected for the calculations. The SG model was built up with a thiophene-like sulfur existing in a pentagonal arrangement (Figure S7, Supporting Information). All the atoms in the model were allowed to relax for all the calculations. The model was also used to demonstrate similar covalent interactions on SG and silicon in our previous work.¹ To describe the interactions between the tin sulfide and SG, the adsorption energies (E_{ads}) were defined by the following equation:

$$E_{\text{ads}} = E_{X\text{-SG}} - E_{\text{SG}} - E_X \quad (3)$$

where $E_{X\text{-SG}}$ represents the energy of SG–SnS or SG–SnS₂, E_{SG} is the energy of SG, and E_X represents the energy of SnS or SnS₂. We studied the adsorption of SnS or SnS₂ on different sites of SG. For the adsorption of SnS₂ on SG, three adsorption configurations (where SnS₂ is located on different sites near the sulfur atom and the adjacent defects) are exhibited in Figure 7a–c, respectively. It was found that covalent interactions are more likely to form between SnS₂ and the C defects, with the highest adsorption energy of –1.05 eV (Figure 7c). In this regard, the S-doping induced C defects in the SG function as active sites for the SnS₂ adsorption. Similarly, parts d–f of Figure 7 present three optimized SnS adsorption configurations on SG. The results show that there is no direct bonding between the SnS and SG structures when SnS is placed on sites that are away from the sulfur and defect site (Figure 7d). The corresponding adsorption energy (–0.36 eV) was contributed mainly by van der Waals interactions. However, at the S-doped defect site, C–S and C–Sn covalent bonding can be observed. Depending on the SnS adsorption configurations, the

adsorption energies vary from -1.23 eV (Figure 7e) to -2.25 eV (Figure 7f). The results further show that the calculated SnS adsorption energies are larger than those of SnS₂, indicating the stronger covalent interaction of SnS adsorption on SG. This can provide evidence for the long life cycle stability of SnS–SG as an anode material in LIBs, as confirmed in Figure 4e. The presence of defects in SG, in addition to stronger affinity of SnS adsorption, presents an explanation for both the higher capacity and the long cycle stability. There has been evidence that Li adsorption to graphene increases as the defects increase, giving rise to higher lithium storage.⁶⁴ The higher adsorption affinity of Sn for SG enhances the stability as, during lithiation/delithiation, there will be minimization for agglomeration. To have a better understanding of the electron structure of the bonding between SnS₂ (or SnS) and SG substrates, the projected density of states (PDOS) of the Sn, S, and C atoms involved in the adsorption were calculated. As shown in Figure 7g,h, there are significant p–p overlaps between the S p and C p states at the whole energy level (from 0 to -10 eV) in SG, showing the strong interaction between S and C atoms. Similarly, the orbital overlaps in Sn–C bonding are mainly contributed by the Sn p and C p states (Figure 7h). The analysis of the PDOS reveals that formation of adsorption bonding between SnS and SG was mainly due to the mixing among the C p, Sn p, and S p states.

CONCLUSIONS

In summary, for the first time, 1D single-crystal, orthorhombic SnS nanorods supported on SG (SnS–SG) were synthesized, showing excellent Li⁺ storage properties and long-term cycling stability. The as-prepared SnS–SG exhibited an excellent rate performance and can deliver 85% capacity retention after 1500 cycles at 1 C. The anisotropic 1D coupled with single-crystal structure of SnS nanorods not only possesses facile strain relaxation, leading to an improved mechanical stability, but also shortens the Li⁺ diffusion paths and the electron transport length. In addition, it is believed that the strategy of synthesizing SnS–SG through heat treatment after employing GO as an oxidizer may open a new way for the synthesis of sulfide-doped graphene to obtain enhanced properties for the storage of Li⁺.

MATERIALS AND METHODS

Materials. Graphene oxide (GO), tin chloride dehydrate (SnCl₂·2H₂O), thiourea, and ethylene glycol (EG) were used in the syntheses. All reagents were of analytical grade and used as received without any purification process.

Synthesis of SnS_x–SG Nanocomposites. GO was fabricated according to previous literature procedures. To synthesize SnS_x–SG nanocomposites, a mixture of GO, EG, SnCl₂·2H₂O, and thiourea was prepared. In a typical synthesis, 90 mg of GO was sonicated in 20 mL. Simultaneously, 0.8 g of thiourea and 400 mg of tin(II) chloride were dissolved separately in 5 mL of DDI each. Then the thiourea and the tin(II) chloride solutions were mixed with the GO solution, and sonication was continued until complete mixing. The above suspension was transferred into an autoclave, and the solution was heated for 10 h at 100 °C and 10 h at 200 °C. After that, the autoclave was cooled to room temperature, and the products were collected and filtered. Then the products were freeze-dried (Labconco Freezone 1, United States) for two nights, and the material is denoted as SnS₂–SG. After that, the SnS₂–SG material was annealed in an argon atmosphere at 500 °C for 3 h followed by furnace cooling, and the resulting material is denoted as SnS–SG.

Reference Material Synthesis. The reference materials containing SnS₂, SnS, and SG were also prepared by the following procedures.

A mixture of EG, SnCl₂·2H₂O, and thiourea was prepared. The above suspension was transferred into an autoclave, and the solution was heated at 100 °C for 10 h and at 200 °C for 10 h. After that, the autoclave was cooled to room temperature, and the products were collected and filtered. Then the products were freeze-dried, and the resulting material is denoted as SnS₂. After that, the SnS₂ was annealed in the furnace under an argon atmosphere at 500 °C for 3 h followed by furnace cooling, and the material is denoted as SnS. For SG, ethylene glycol, graphene oxide, and thiourea were mixed by sonication and then subjected to the same solvothermal method as mentioned above.

Materials Characterization. X-ray diffraction (XRD) patterns were collected using Ni-filtered Cu K α radiation ($\lambda = 1.5418$ Å). The morphology of the nanocomposites was observed using a field emission scanning electron microscopy (FE-SEM) instrument (Zeiss Ultra Plus, United Kingdom) and a high-resolution transmission electron microscopy (HRTEM) instrument (FEI Philips CM 300, United States). Thermal gravimetric analysis (TGA) was carried out to explore the ratio of tin sulfides and graphene. TGA was conducted in air at a heat ramp of 10 °C min⁻¹ to 800 °C. X-ray photoelectron spectroscopy (XPS) was also used to confirm the composition of SnS_x–SG and SG products.

Electrochemical Evaluation. The working electrodes were fabricated by mixing 60 wt % active material, 20 wt % super P (as a carbon additive for conductivity enhancement), and 20 wt % CMC and PAA (weight ratio 1:1) (used as a binder, 2 wt % CMC (sodium carboxymethyl cellulose) in water and poly(acrylic acid), Sigma-Aldrich) and coated on copper foils. The average mass loading of the active materials in the electrode was maintained around 2.1 mg cm⁻². The electrodes were treated in a vacuum oven for 2 h at 150 °C and assembled in a glovebox (MBRAUN 10, United States). Conventional two-electrode coin cells were fabricated using lithium metal (Aldrich, United States) as the counter electrode and LiPF₆ (1 M) in ethylene carbonate/diethyl carbonate (EC/DEC; 3:7, vol %) as the electrolyte. The electrochemical performances of the prepared electrodes were characterized by cyclic voltammetry (Versa Stat MC, Princeton Applied Research, United States) and galvanostatic charge–discharge (Neware, China) tests between 0.1 and 3 V vs Li/Li⁺. All of the specific capacities in this study were calculated on the basis of the mass of active materials (SnS_x–SG).

ASSOCIATED CONTENT

Supporting Information

The Supporting Information is available free of charge on the ACS Publications website at DOI: 10.1021/acsami.7b04483.

Schematic of the structure phase transformation of SnS–SG (Figure S1), SEM images of the nonsupported SnS₂ and SnS (Figure S2), characterization of sulfur-doped graphene (Figure S3), rate capability of the different electrode materials (Figure S4), voltage profile for SnS₂–SG, SnS₂, and SG (Figure S5), voltage profile of SnS₂–SG at different current densities (Figure S6), DFT-optimized geometry of SG (Figure S7), and estimation of the expected capacity of the hybrid material (PDF)

AUTHOR INFORMATION

Corresponding Authors

*E-mail: xingcheng.xiao@gm.com.

*E-mail: zhwenchen@uwaterloo.ca.

ORCID

Zhongwei Chen: 0000-0003-3463-5509

Notes

The authors declare no competing financial interest.

ACKNOWLEDGMENTS

We acknowledge financial support from the Natural Sciences and Engineering Research Council of Canada (NSERC), the University of Waterloo, and the Waterloo Institute for Nanotechnology. TEM and HAADF-STEM images were obtained at the Canadian Center for Electron Microscopy (CCEM) located at McMaster University, thanks to Dr. Carmen Andrei.

REFERENCES

- (1) Hassan, F. M.; Batmaz, R.; Li, J.; Wang, X.; Xiao, X.; Yu, A.; Chen, Z. Evidence of Covalent Synergy in Silicon-Sulfur-Graphene Yielding Highly Efficient and Long-Life Lithium-Ion Batteries. *Nat. Commun.* **2015**, *6*, 8597.
- (2) Hassan, F. M.; Chen, Z.; Yu, A.; Chen, Z.; Xiao, X. Sn/SnO₂ Embedded in Mesoporous Carbon Nanocomposites as Negative Electrode for Lithium Ion Batteries. *Electrochim. Acta* **2013**, *87*, 844–852.
- (3) Liao, J.-Y.; Higgins, D.; Lui, G.; Chabot, V.; Xiao, X.; Chen, Z. Multifunctional TiO₂-C/MnO₂ Core-Double-Shell Nanowire Arrays as High-Performance 3d Electrodes for Lithium Ion Batteries. *Nano Lett.* **2013**, *13*, 5467–5473.
- (4) Tarascon, J. M.; Armand, M. Issues and Challenges Facing Rechargeable Lithium Batteries. *Nature* **2001**, *414*, 359–367.
- (5) Machado, B. F.; Serp, P. Graphene-Based Materials for Catalysis. *Catal. Sci. Technol.* **2012**, *2*, 54–75.
- (6) Liao, J.-Y.; Xiao, X.; Higgins, D.; Lee, D.; Hassan, F.; Chen, Z. Hierarchical Li₄Ti₅O₁₂-TiO₂ Composite Microsphere Consisting of Nanocrystals for High Power Li-Ion Batteries. *Electrochim. Acta* **2013**, *108*, 104–111.
- (7) Hassan, F. M.; Chabot, V.; Elsayed, A. R.; Xiao, X.; Chen, Z. Engineered Si Electrode Nanoarchitecture: A Scalable Postfabrication Treatment for the Production of Next-Generation Li-Ion Batteries. *Nano Lett.* **2014**, *14*, 277–283.
- (8) Hassan, F. M.; Elsayed, A. R.; Chabot, V.; Batmaz, R.; Xiao, X.; Chen, Z. Subeutectic Growth of Single-Crystal Silicon Nanowires Grown on and Wrapped with Graphene Nanosheets: High-Performance Anode Material for Lithium-Ion Battery. *ACS Appl. Mater. Interfaces* **2014**, *6*, 13757–13764.
- (9) Jian, Z.; Zheng, M.; Liang, Y.; Zhang, X.; Gheyfani, S.; Lan, Y.; Shi, Y.; Yao, Y. Li₃VO₄ Anchored Graphene Nanosheets for Long-Life and High-Rate Lithium-Ion Batteries. *Chem. Commun.* **2015**, *51*, 229–231.
- (10) Liu, N.; Wu, H.; McDowell, M. T.; Yao, Y.; Wang, C.; Cui, Y. A Yolk-Shell Design for Stabilized and Scalable Li-Ion Battery Alloy Anodes. *Nano Lett.* **2012**, *12*, 3315–3321.
- (11) Yao, Y.; McDowell, M. T.; Ryu, I.; Wu, H.; Liu, N.; Hu, L.; Nix, W. D.; Cui, Y. Interconnected Silicon Hollow Nanospheres for Lithium-Ion Battery Anodes with Long Cycle Life. *Nano Lett.* **2011**, *11*, 2949–2954.
- (12) Xiao, J.; Zheng, J.; Li, X.; Shao, Y.; Zhang, J.-G. Hierarchically Structured Materials for Lithium Batteries. *Nanotechnology* **2013**, *24*, 424004.
- (13) Chen, X.; Li, X.; Ding, F.; Xu, W.; Xiao, J.; Cao, Y.; Meduri, P.; Liu, J.; Graff, G. L.; Zhang, J.-G. Conductive Rigid Skeleton Supported Silicon as High-Performance Li-Ion Battery Anodes. *Nano Lett.* **2012**, *12*, 4124–4130.
- (14) Kim, G.; Jeong, S.; Shin, J.-H.; Cho, J.; Lee, H. 3D Amorphous Silicon on Nanopillar Copper Electrodes as Anodes for High-Rate Lithium-Ion Batteries. *ACS Nano* **2014**, *8*, 1907–1912.
- (15) Jeong, S.; Lee, J.-P.; Ko, M.; Kim, G.; Park, S.; Cho, J. Etched Graphite with Internally Grown Si Nanowires from Pores as an Anode for High Density Li-Ion Batteries. *Nano Lett.* **2013**, *13*, 3403–3407.
- (16) Chao, D.; Liang, P.; Chen, Z.; Bai, L.; Shen, H.; Liu, X.; Xia, X.; Zhao, Y.; Savilov, S. V.; Lin, J.; Shen, Z. X. Pseudocapacitive Na-Ion Storage Boosts High Rate and Areal Capacity of Self-Branched 2D Layered Metal Chalcogenide Nanoarrays. *ACS Nano* **2016**, *10*, 10211–10219.
- (17) Gewirth, A. A.; Thorum, M. S. Electroreduction of Dioxide for Fuel-Cell Applications: Materials and Challenges. *Inorg. Chem.* **2010**, *49*, 3557–3566.
- (18) Gao, M.-R.; Jiang, J.; Yu, S.-H. Catalysis: Solution-Based Synthesis and Design of Late Transition Metal Chalcogenide Materials for Oxygen Reduction Reaction (ORR). *Small* **2012**, *8*, 12–12.
- (19) Sigala, C.; Guyomard, D.; Verbaere, A.; Piffard, Y.; Tournoux, M. Positive Electrode Materials with High Operating Voltage for Lithium Batteries: LiCr_yMn_{2-y}O₄ (0 ≤ y ≤ 1). *Solid State Ionics* **1995**, *81*, 167–170.
- (20) Xiao, J.; Choi, D.; Cosimbescu, L.; Koech, P.; Liu, J.; Lemmon, J. P. Exfoliated MoS₂ Nanocomposite as an Anode Material for Lithium Ion Batteries. *Chem. Mater.* **2010**, *22*, 4522–4524.
- (21) Jiang, Y.; Feng, Y.; Xi, B.; Kai, S.; Mi, K.; Feng, J.; Zhang, J.; Xiong, S. Ultrasmall SnS₂ Nanoparticles Anchored on Well-Distributed Nitrogen-Doped Graphene Sheets for Li-Ion and Na-Ion Batteries. *J. Mater. Chem. A* **2016**, *4*, 10719–10726.
- (22) Hwang, H.; Kim, H.; Cho, J. MoS₂ Nanoplates Consisting of Disordered Graphene-Like Layers for High Rate Lithium Battery Anode Materials. *Nano Lett.* **2011**, *11*, 4826–4830.
- (23) Lai, C.-H.; Lu, M.-Y.; Chen, L.-J. Metal Sulfide Nanostructures: Synthesis, Properties and Applications in Energy Conversion and Storage. *J. Mater. Chem.* **2012**, *22*, 19–30.
- (24) Jiang, Y.; Wei, M.; Feng, J.; Ma, Y.; Xiong, S. Enhancing the Cycling Stability of Na-Ion Batteries by Bonding SnS₂ Ultrafine Nanocrystals on Amino-Functionalized Graphene Hybrid Nanosheets. *Energy Environ. Sci.* **2016**, *9*, 1430–1438.
- (25) Choi, N.-S.; Yao, Y.; Cui, Y.; Cho, J. One Dimensional Si/Sn - Based Nanowires and Nanotubes for Lithium-Ion Energy Storage Materials. *J. Mater. Chem.* **2011**, *21*, 9825–9840.
- (26) Kim, T.-J.; Kim, C.; Son, D.; Choi, M.; Park, B. Novel SnS₂-Nanosheet Anodes for Lithium-Ion Batteries. *J. Power Sources* **2007**, *167*, 529–535.
- (27) Liu, S.; Lu, X.; Xie, J.; Cao, G.; Zhu, T.; Zhao, X. Preferential C-Axis Orientation of Ultrathin SnS₂ Nanoplates on Graphene as High-Performance Anode for Li-Ion Batteries. *ACS Appl. Mater. Interfaces* **2013**, *5*, 1588–1595.
- (28) Luo, B.; Fang, Y.; Wang, B.; Zhou, J.; Song, H.; Zhi, L. Two Dimensional Graphene-SnS₂ Hybrids with Superior Rate Capability for Lithium Ion Storage. *Energy Environ. Sci.* **2012**, *5*, 5226–5230.
- (29) Mei, L.; Xu, C.; Yang, T.; Ma, J.; Chen, L.; Li, Q.; Wang, T. Superior Electrochemical Performance of Ultrasmall SnS₂ Nanocrystals Decorated on Flexible RGO in Lithium-Ion Batteries. *J. Mater. Chem. A* **2013**, *1*, 8658–8664.
- (30) Cai, J.; Li, Z.; Shen, P. K. Porous Sn Nanorods/Carbon Hybrid Materials as Highly Stable and High Capacity Anode for Li-Ion Batteries. *ACS Appl. Mater. Interfaces* **2012**, *4*, 4093–4098.
- (31) Kang, J.-G.; Park, J.-G.; Kim, D.-W. Superior Rate Capabilities of SnS Nanosheet Electrodes for Li Ion Batteries. *Electrochem. Commun.* **2010**, *12*, 307–310.
- (32) Li, Y.; Tu, J. P.; Huang, X. H.; Wu, H. M.; Yuan, Y. F. Net-Like SnS/Carbon Nanocomposite Film Anode Material for Lithium Ion Batteries. *Electrochem. Commun.* **2007**, *9*, 49–53.
- (33) Vaughn, D. D.; Hentz, O. D.; Chen, S.; Wang, D.; Schaak, R. E. Formation of SnS Nanoflowers for Lithium Ion Batteries. *Chem. Commun.* **2012**, *48*, 5608–5610.
- (34) Conway, B. E.; Wilkinson, D. P. Non-Isothermal Cell Potentials and Evaluation of Entropies of Ions and of Activation for Single Electrode Processes in Non-Aqueous Media. *Electrochim. Acta* **1993**, *38*, 997–1013.
- (35) Pan, D.; Spanu, L.; Harrison, B.; Sverjensky, D. A.; Galli, G. Dielectric Properties of Water under Extreme Conditions and Transport of Carbonates in the Deep Earth. *Proc. Natl. Acad. Sci. U. S. A.* **2013**, *110*, 6646–6650.
- (36) Xia, Y.; Xiong, Y.; Lim, B.; Skrabalak, S. E. Shape-Controlled Synthesis of Metal Nanocrystals: Simple Chemistry Meets Complex Physics? *Angew. Chem., Int. Ed.* **2009**, *48*, 60–103.
- (37) Higgins, D. C.; Hassan, F. M.; Seo, M. H.; Choi, J. Y.; Hoque, M. A.; Lee, D. U.; Chen, Z. Shape-Controlled Octahedral Cobalt

Disulfide Nanoparticles Supported on Nitrogen and Sulfur-Doped Graphene/Carbon Nanotube Composites for Oxygen Reduction in Acidic Electrolyte. *J. Mater. Chem. A* **2015**, *3*, 6340–6350.

(38) Bayoumi, F. M. Kinetics of High Temperature Corrosion of a Low Cr-Mo Steel in Aqueous NaCl Solution. *Mater. Corros.* **2007**, *58*, 422–426.

(39) Zhang, M.; Lei, D.; Du, Z.; Yin, X.; Chen, L.; Li, Q.; Wang, Y.; Wang, T. Fast Synthesis of SnO₂/Graphene Composites by Reducing Graphene Oxide with Stannous Ions. *J. Mater. Chem.* **2011**, *21*, 1673–1676.

(40) Liu, S.; Yin, X.; Chen, L.; Li, Q.; Wang, T. Synthesis of Self-Assembled 3D Flowerlike SnS₂ Nanostructures with Enhanced Lithium Ion Storage Property. *Solid State Sci.* **2010**, *12*, 712–718.

(41) Zhou, T.; Pang, W. K.; Zhang, C.; Yang, J.; Chen, Z.; Liu, H. K.; Guo, Z. Enhanced Sodium-Ion Battery Performance by Structural Phase Transition from Two-Dimensional Hexagonal-SnS₂ to Orthorhombic-Sns. *ACS Nano* **2014**, *8*, 8323–8333.

(42) Biacchi, A. J.; Vaughn, D. D.; Schaak, R. E. Synthesis and Crystallographic Analysis of Shape-Controlled Sns Nanocrystal Photocatalysts: Evidence for a Pseudotetragonal Structural Modification. *J. Am. Chem. Soc.* **2013**, *135*, 11634–11644.

(43) Shchukarev, A. V.; Korolkov, D. V. XPS Study of Group Ia Carbonates. *Cent. Eur. J. Chem.* **2004**, *2*, 347–362.

(44) Yang, Z.; Yao, Z.; Li, G.; Fang, G.; Nie, H.; Liu, Z.; Zhou, X.; Chen, X. a.; Huang, S. Sulfur-Doped Graphene as an Efficient Metal-Free Cathode Catalyst for Oxygen Reduction. *ACS Nano* **2012**, *6*, 205–211.

(45) Chia, X.; Lazar, P.; Sofer, Z.; Luxa, J.; Pumera, M. Layered Sns Versus SnS₂: Valence and Structural Implications on Electrochemistry and Clean Energy Electrocatalysis. *J. Phys. Chem. C* **2016**, *120*, 24098–24111.

(46) Ferrari, A. C.; Meyer, J. C.; Scardaci, V.; Casiraghi, C.; Lazzeri, M.; Mauri, F.; Piscanec, S.; Jiang, D.; Novoselov, K. S.; Roth, S.; Geim, A. K. Raman Spectrum of Graphene and Graphene Layers. *Phys. Rev. Lett.* **2006**, *97*, 187401.

(47) Lin, W.; Moon, K.-S.; Zhang, S.; Ding, Y.; Shang, J.; Chen, M.; Wong, C.-p. Microwave Makes Carbon Nanotubes Less Defective. *ACS Nano* **2010**, *4*, 1716–1722.

(48) Van Ginkel, C. G.; Gayton, S. The Biodegradability and Nontoxicity of Carboxymethyl Cellulose (DS 0.7) and Intermediates. *Environ. Toxicol. Chem.* **1996**, *15*, 270–274.

(49) Larson, R. J.; Bookland, E. A.; Williams, R. T.; Yocom, K. M.; Saucy, D. A.; Freeman, M. B.; Swift, G. Biodegradation of Acrylic Acid Polymers and Oligomers by Mixed Microbial Communities in Activated Sludge. *J. Environ. Polym. Degrad.* **1997**, *5*, 41–48.

(50) Datta, D.; Li, J.; Koratkar, N.; Shenoy, V. B. Enhanced Lithiation in Defective Graphene. *Carbon* **2014**, *80*, 305–310.

(51) Nitta, N.; Wu, F.; Lee, J. T.; Yushin, G. Li-Ion Battery Materials: Present and Future. *Mater. Today* **2015**, *18*, 252–264.

(52) Choi, S.; Kang, Y. Aerosol-Assisted Rapid Synthesis of SnS-C Composite Microspheres as Anode Material for Na-Ion Batteries. *Nano Res.* **2015**, *8*, 1595–1603.

(53) Zhu, J.; Wang, D.; Liu, T. Preparation of Tin Sulfide-Graphene Composites with Enhanced Lithium Storage. *Appl. Surf. Sci.* **2013**, *282*, 947–953.

(54) Du, Y.; Yin, Z.; Rui, X.; Zeng, Z.; Wu, X.-J.; Liu, J.; Zhu, Y.; Zhu, J.; Huang, X.; Yan, Q.; Zhang, H. A Facile, Relative Green, and Inexpensive Synthetic Approach toward Large-Scale Production of SnS₂ Nanoplates for High-Performance Lithium-Ion Batteries. *Nano-scale* **2013**, *5*, 1456–1459.

(55) Kim, H. S.; Chung, Y. H.; Kang, S. H.; Sung, Y.-E. Electrochemical Behavior of Carbon-Coated SnS₂ for Use as the Anode in Lithium-Ion Batteries. *Electrochim. Acta* **2009**, *54*, 3606–3610.

(56) Morales, J.; Perez-Vicente, C.; Tirado, J. L. Chemical and Electrochemical Lithium Intercalation and Staging in 2H-SnS₂. *Solid State Ionics* **1992**, *51*, 133–138.

(57) Lefebvre-Devos, I.; Olivier-Fourcade, J.; Jumas, J. C.; Lavela, P. Lithium Insertion Mechanism in SnS₂. *Phys. Rev. B: Condens. Matter Mater. Phys.* **2000**, *61*, 3110–3116.

(58) Li, Y.; Chen, Z. XH/ π (X = C, Si) Interactions in Graphene and Silicene: Weak in Strength, Strong in Tuning Band Structures. *J. Phys. Chem. Lett.* **2013**, *4*, 269–275.

(59) Marsoner Steinkasserer, L. E.; Paulus, B.; Voloshina, E. Impact of the Metal Substrate on the Electronic Structure of Armchair Graphene Nanoribbons. *Chem. Phys. Lett.* **2014**, *597*, 148–152.

(60) Arabi, A. A.; Becke, A. D. Assessment of the PW86+PBE+XDM Density Functional on Van Der Waals Complexes at Non-Equilibrium Geometries. *J. Chem. Phys.* **2012**, *137*, 014104.

(61) te Velde, G.; Baerends, E. J. Precise Density-Functional Method for Periodic Structures. *Phys. Rev. B: Condens. Matter Mater. Phys.* **1991**, *44*, 7888–7903.

(62) Wiesenekker, G.; Baerends, E. J. Quadratic Integration over the Three-Dimensional Brillouin Zone. *J. Phys.: Condens. Matter* **1991**, *3*, 6721.

(63) Grimme, S.; Antony, J.; Ehrlich, S.; Krieg, H. A Consistent and Accurate Ab Initio Parametrization of Density Functional Dispersion Correction (DFT-D) for the 94 Elements H-Pu. *J. Chem. Phys.* **2010**, *132*, 154104.

(64) Sun, X.; Wang, Z.; Fu, Y. Q. Defect-Mediated Lithium Adsorption and Diffusion on Monolayer Molybdenum Disulfide. *Sci. Rep.* **2016**, *5*, 18712.